Shock Waves (2016) 26:161–168
DOI 10.1007/s00193-015-0600-5

ORIGINAL ARTICLE

Structure of an oblique detonation wave induced by a wedge

Y. Liu[1] · Y.-S. Liu[1] · D. Wu[1] · J.-P. Wang[1]

Received: 1 February 2015 / Revised: 15 September 2015 / Accepted: 23 September 2015 / Published online: 12 October 2015

Abstract The structure of an oblique detonation wave (ODW) induced by a wedge is investigated via numerical simulations and Rankine–Hugoniot analysis. The two-dimensional Euler equations coupled with a two-step chemical reaction model are solved. In the numerical results, four configurations of the Chapman–Jouguet (CJ) ODW reflection (overall Mach reflection, Mach reflection, regular reflection, and non-reflection) are observed to take place sequentially as the inflow Mach number increases. According to the numerical and analytical results, the change of the CJ ODW reflection configuration results from the interaction among the ODW, the CJ ODW, and the centered expansion wave.

Keywords Oblique detonation wave · CJ ODW · Reflection configuration · Centered expansion wave

Abbreviations

ODW	Oblique detonation wave
OSW	Oblique shock wave
CJ ODW	Chapman–Jouguet oblique detonation wave (which locates at the end of the induction region)
CEW	Centered expansion wave (which locates behind the CJ ODW)
RCEW	Reflected expansion wave of the CEW
ROSW	Reflected shock wave of the OSW
RCJ ODW	Reflected shock wave of the CJ ODW

Communicated by A. Sasoh and A. Higgins.

✉ Y. Liu
liuyandeyoux@126.com

Y.-S. Liu
lylcbef@126.com

D. Wu
wudan65@126.com

J.-P. Wang
wangjp@pku.edu.cn

[1] Center for Combustion and Propulsion, SKLTCS, Department of Mechanics and Engineering Science, College of Engineering, Peking University, Beijing 100871, China

1 Introduction

Detonation is a shock-induced combustion wave that propagates with hypersonic velocity and has inherently high thermodynamic efficiency [1,2]. In previous decades, the detonation wave stabilized over a wedge in a supersonic detonable mixture, which is called an oblique detonation wave (ODW), is regarded as a promising combustion mechanism for hypersonic vehicles [3]. Consequently, the ODW has received considerable attention and extensive analytical [4,5], numerical [6–10], and experimental [11,14–16] work has been conducted by prior researchers.

In the numerical simulations of Li et al. [6], the ODW structures consist of an oblique shock wave (OSW), an induction region, a set of deflagration waves, and a reactive shock, namely the ODW front. In the numerical results of Choi et al. [7], it was observed that the front of the ODW became unstable and formed cell-like structures when the activation energy was high enough. Furthermore, the instability of the ODW front became irregular when the activation energy was too high. Wang et al. [8] verified that the transverse waves facing upstream would be formed when the computational domain was long enough. Gui et al. [9] divided the ODW front into

three sections according to the state of the transverse waves, i.e., the Zeldovich–von Neumann–Döring (ZND) model-like structure, the single-sided triple point structure, and the dual-headed triple point structure. Using steady method of characteristics calculations and unsteady computational flow field simulations, Verreault et al. [10] confirmed that the spatial oscillation of the OSW was the origin of the transverse waves facing upstream, and the temporal instability of the spatial oscillation was the origin of the transverse waves facing downstream.

In the experiments of Verreault and Higgins [11], the ODW attached to the cone tip was named a prompt ODW. The ODW that transitioned from an inert OSW was named a delayed ODW. By numerical simulation, Lefebvre and Fujiwara [12] found that the ODW at low inflow Mach number would propagate upstream from its initiation location and eventually stabilize at the cone tip (prompt ODW). According to the numerical and analytical results of Liu et al. [13], the prompt ODW is likely to take place at low inflow Mach number and large wedge angle. In the experiments of Dabora and Broda [14], Viguier et al. [15], and Maeda et al. [16], the delayed ODW was also observed. In these experiments [14–16], the OSW, the induction region, and the ODW were verified, and the induction region was observed to be ended by a detonation wave rather than a set of deflagration waves. According to the analytical study by Ashford and Emanuel [17] and the numerical study by Verreault et al. [18], the detonation wave behind the induction region should be a Chapman–Jouguet (CJ) ODW and followed by a centered expansion wave (CEW). This model was also adopted by Ghorbanian and Sterling [5]. Using this model, they performed a detailed analysis of the ODW in the near field and far field over a variable-double-ramp geometry. According to the numerical results with a detailed chemical reaction model, Teng et al. [19] found that the ODW structures were greatly influenced by the inflow Mach number. However, the formation mechanisms of these ODW structures are still unclear.

In this study, numerical simulations along with Rankine–Hugoniot (R–H) analysis are performed to clarify the formation mechanisms and evolution processes of the ODW structures. A steady and homogeneous inflow is adopted in this study. Even though such an ideal inflow is unrealistic for the ODW in applications, this study is the basis for study of the ODW under real conditions. A two-step chemical reaction model of hydrogen-air is adopted in this study, which allows us to simulate the ODW structures over a wide range of wedge angles and inflow Mach numbers with a high-resolution algorithm. Despite its simplicity, it can reproduce correct ODW structures that qualitatively agree with the experimental results [11,14–16] and numerical results of detailed chemical reaction models [19]. This is another reason we chose this chemical reaction model.

2 Numerical method and physical model

The numerical method and physical model used in this study are the same as those used by Liu et al. [13]. According to the numerical results of Li et al. [20] and the experimental results of Kamel et al. [21], the effects of viscosity are limited to the boundary layer and have little influence on the overall detonation structure. The thickness of the boundary layer in our study is about 1–2 orders of magnitude smaller than the thickness of the induction region. Furthermore, the focus of this study is the interaction among the CJ ODW, ODW, and CEW. The influence of the boundary layer is not important. Therefore, in the numerical simulations, the effects of viscosity, thermal conduction, and mass diffusion are assumed to be negligible. The two-dimensional Euler equations coupled with the two-step chemical reaction model developed by Korobeinikov et al. [22] are solved. The governing equations are

$$\frac{\partial \boldsymbol{U}}{\partial t}+\frac{\partial \boldsymbol{E}}{\partial x}+\frac{\partial \boldsymbol{F}}{\partial y}=\boldsymbol{S} \tag{1}$$

$$\boldsymbol{U}=\begin{bmatrix}\rho\\ \rho u\\ \rho v\\ e\\ \rho\beta\\ \rho\alpha\end{bmatrix},\quad \boldsymbol{E}=\begin{bmatrix}\rho u\\ \rho u^2+p\\ \rho uv\\ (e+p)u\\ \rho u\beta\\ \rho u\alpha\end{bmatrix},$$

$$\boldsymbol{F}=\begin{bmatrix}\rho v\\ \rho uv\\ \rho v^2+p\\ (e+p)v\\ \rho v\beta\\ \rho v\alpha\end{bmatrix},\quad \boldsymbol{S}=\begin{bmatrix}0\\ 0\\ 0\\ 0\\ \rho\omega_\beta\\ \rho\omega_\alpha\end{bmatrix} \tag{2}$$

where ρ, p, u, and v are the density, pressure, and velocity components along the x and y coordinates, respectively. e is the total energy per unit volume, defined as:

$$e=\frac{p}{\gamma-1}+\beta\rho q+\frac{1}{2}\rho(u^2+v^2) \tag{3}$$

where α and β are the progress variables of the induction reaction and exothermic reaction, respectively. α decreases from unity in the induction region. β decreases from unity when α goes below zero. The chemical reaction rates are given by

$$\omega_\alpha=\frac{\mathrm{d}\alpha}{\mathrm{d}t}=-k_1\rho\exp(-E_1/RT) \tag{4}$$

$$\omega_\beta=\frac{\mathrm{d}\beta}{\mathrm{d}t}=\begin{cases}-k_2p^2\left[\beta^2\exp\left(\frac{-E_2}{RT}\right)\right.\\ \left.-(1-\beta)^2\exp\left(-\frac{E_2+q}{RT}\right)\right] & (\alpha\le 0)\\ 0 & (0<\alpha\le 1)\end{cases} \tag{5}$$

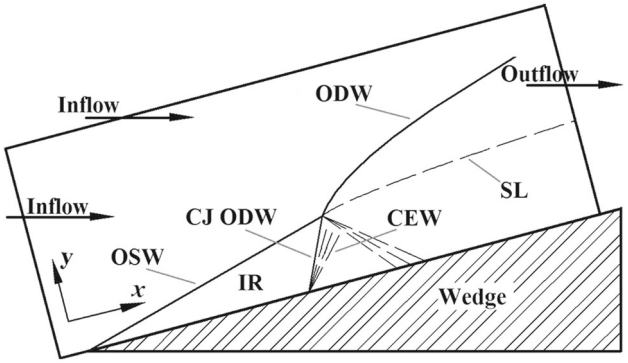

Fig. 1 Schematic of the computational domain and structure of the ODW proposed by Ghorbanian and Sterling [5]. *IR* Induction region, *SL* Shear layer

where E_1, E_2, k_1, and k_2 are the same as those of Liu [23] for stoichiometric hydrogen–air mixtures. In this study, the temperature and pressure of the incoming mixtures are 292 K and 1 atm, respectively.

The flux vectors are split by a Steger–Warming approach [24]. The split flux vectors are integrated by the fifth-order weighted essentially nonoscillatory (WENO) scheme [25]. The third-order Runge–Kutta scheme is adopted to integrate the discretized equations in time.

Figure 1 shows the schematic of the computational domain and structure of the ODW proposed by Ghorbanian and Sterling [5]. The computational domain is the rectangle above the wedge surface as illustrated in Fig. 1. The axes x and y are parallel and vertical to the wedge surface, respectively. At the left and the upper boundaries, the inflow boundary conditions are fixed at the initial values. At the wedge surface, a slip boundary condition is adopted. A zero-gradient condition is imposed to the right boundary and the first part of the bottom boundary.

All the calculations presented in this study are performed using a uniform mesh in both directions, and the grid size Δx is fixed at 0.02 mm. The ratio of Δx to the induction length of an ideal ZND detonation is 0.17. To test the convergence of the grid system, three levels of grid resolution are adopted. Figure 2a–c shows the pressure fields of the ODWs at $M = 8.0$ and $\theta = 23°$ with $\Delta x = 0.04$ mm, 0.02 mm, and 0.01 mm. The numbers of the grid points in these three cases are 1800×800, 3600×1600, and 7200×3200, respectively. The wave angles of the CJ ODWs are in good agreement, and are 47.4°, 47.7°, and 47.5°, respectively. They compare well with the value obtained by R–H analysis, 49°. The pressure profiles along $y = 1$ mm of the ODWs are illustrated in Fig. 2d. As observed in Fig. 2d, the CJ ODW and the reflected shock wave of the CJ ODW (RCJ ODW) at $\Delta x = 0.02$ mm are in good agreement with those at $\Delta x = 0.01$ mm. Therefore, it can be

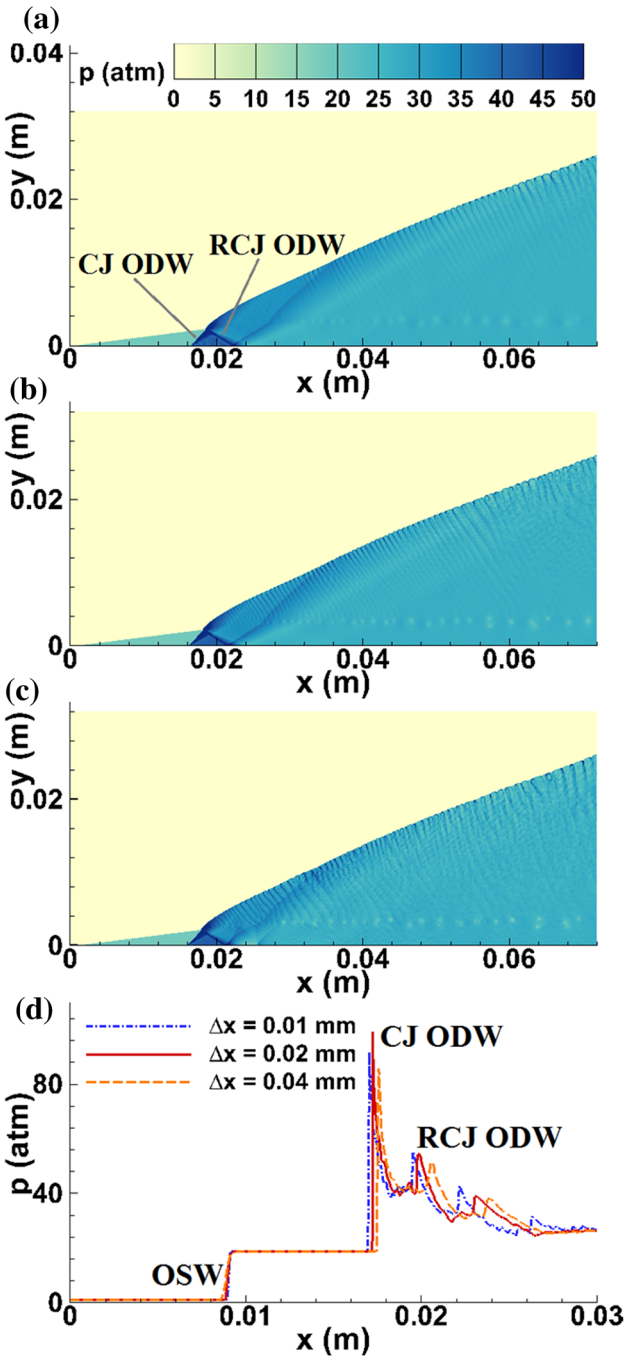

Fig. 2 Pressure fields of the ODW at $M = 8.0$ and $\theta = 23°$ with $\Delta x =$ **a** 0.04 mm, **b** 0.02 mm, and **c** 0.01 mm. The pressure profiles in the fourth panel are plotted along $y = 1$ mm

concluded that the major structures are well resolved with $\Delta x = 0.02$ mm, which guarantees the reliability of our conclusions. In addition, with $\Delta x = 0.02$ mm and 0.01 mm, the cell-like structures are both well resolved. As a consequence, the grid size $\Delta x = 0.02$ mm is adopted in this study.

3 Results and discussion

3.1 R–H analysis of the ODW and CJ ODW

Figure 3 shows the shock polars of the ODWs and the CJ ODWs at $M = 7.0$, 8.0, and 9.0. They are obtained by solving the R–H equations and the chemical equilibrium equation, $\omega_\beta = 0$. The equations are calculated as follows:

$$\rho_0 u_{0n} = \rho_1 u_{1n} \tag{6}$$

$$(\rho_0 u_{0n}) u_{0t} = (\rho_1 u_{1n}) u_{1t} \tag{7}$$

$$p_0 + \rho_0 u_{0n}^2 = p_1 + \rho_1 u_{1n}^2 \tag{8}$$

$$c_p T_0 + \left(1 - \beta_{\text{eq}}\right) q + u_{0n}^2/2 = c_p T_1 + u_{1n}^2/2 \tag{9}$$

$$\beta_{\text{eq}} = \frac{1}{1 + \exp\left(q/2RT_1\right)} \tag{10}$$

The subscripts 0 and 1 denote the upstream and downstream conditions, respectively. The subscripts t and n refer to flow tangential and normal to the shock wave, respectively. A complete description of this method is given by Pratt et al. [4], Ghorbanian and Sterling [5], and Liu et al. [13].

As shown in Fig. 1, the combustion products of the CJ ODW are pressurized by two shock waves, the OSW and the CJ ODW. As a result, the post-shock pressure P_{CJODW} of the CJ ODW is always higher than the post-shock pressure P_{ODW} and the detachment pressure $P_{\text{det,ODW}}$ of the ODW as observed in Fig. 3. In the ODW structures proposed by Ghorbanian and Sterling [5] as shown in Fig. 1, the CJ ODW and ODW are directly linked, and their combustion products are separated by a shear layer that cannot tolerate any pressure difference. Therefore, a convex ODW in the vicinity of the CJ ODW is always formed to balance the high pressure of the CJ ODW combustion products, i.e., the ODW is strengthened. This phenomenon has been observed in other experimental [14–16] and numerical [6,13,19] results as well as our numerical results. In the next section, it will be found that the CJ ODW itself receives feedback from the strengthened ODW as well.

As observed in Fig. 3, P_{CJODW} and $P_{\text{det,ODW}}$ both increase with increasing M, but the increase of $P_{\text{det,ODW}}$ is faster. Therefore, the difference between the P_{CJODW} and $P_{\text{det,ODW}}$ decreases with increasing M. For instance, the ratios of P_{CJODW} to $P_{\text{det,ODW}}$ at $\theta = 25°$ and $M = 7.0$, 7.5, 8.4, and 9.0 are 1.88, 1.68, 1.41, and 1.28, respectively. As a result of this decreasing pressure difference, the interaction between the CJ ODW and the ODW should become weaker with an increase of M. This tendency is observed in the following numerical results.

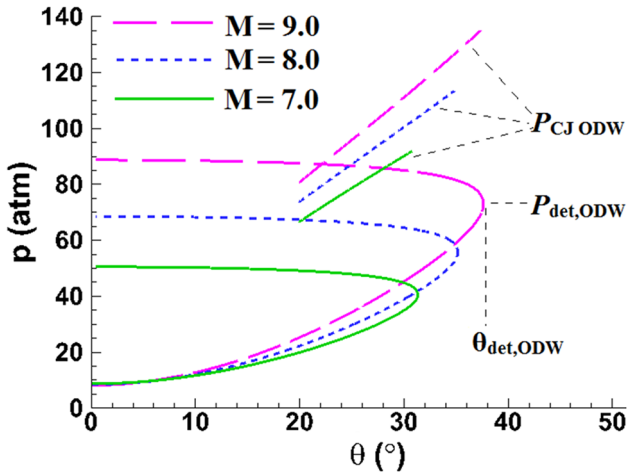

Fig. 3 Polars of the ODW and CJ ODW: pressure vs. wedge angle

3.2 Numerical results of ODW structures

Figure 4 shows the pressure field and pressure profiles along the constant y coordinates of the ODW at $\theta = 25°$ and $M = 7.0$. To clearly illustrate the salient features of the ODW structures, only the flow field within $x < 3.6$ cm is shown in Fig. 4. Identical to the R–H analysis results, the post-shock pressure of the CJ ODW shown in Fig. 4 is much higher than that of the ODW. To balance the high pressure of the CJ ODW combustion products, a convex ODW in the vicinity of the

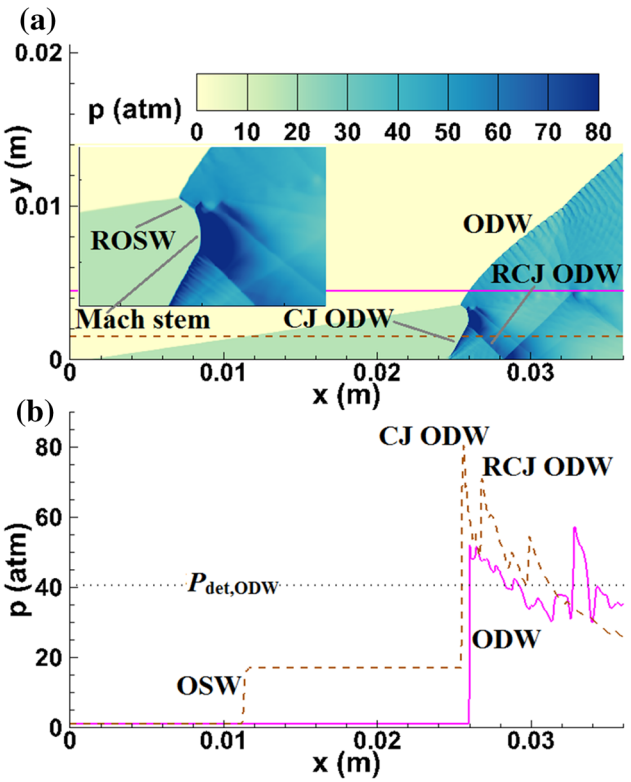

Fig. 4 Pressure field and pressure profiles of the ODW at $\theta = 25°$ and $M = 7.0$. The pressure profiles in the *second panel* are plotted *along the lines* shown in the *first panel*

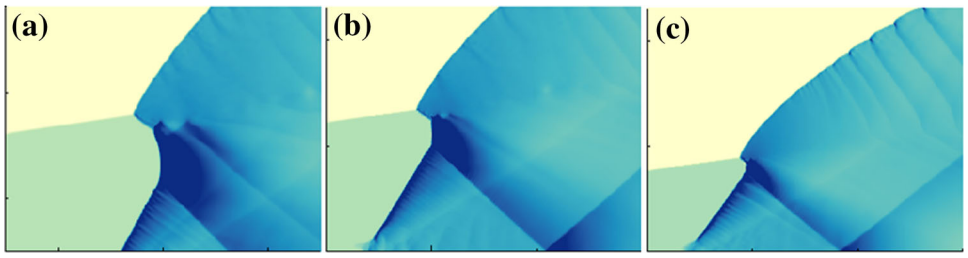

Fig. 5 Pressure fields near the CJ ODW at wedge angle $\theta = 25°$ and $M =$ **a** 7.0, **b** 7.2, and **c** 7.5

CJ ODW is formed as observed in Fig. 4a. Similar to normal detonation waves, the post-shock pressures of the ODW and the CJ ODW both decrease quickly. However, as observed in Fig. 4b, there is still a region behind the ODW in which the pressure is higher than its detachment pressure $P_{\mathrm{det,ODW}}$. As a result, the ODW is detached from the link point between itself and the CJ ODW. Then, the reflected shock wave of the OSW (ROSW) is formed, and then the ODW and the CJ ODW are linked by this reflected shock wave. As shown in Fig. 4a, the ROSW and the CJ ODW are not smoothly linked. Instead, a Mach stem is formed between them. In addition, the reflected shock waves are both observed in the flow field, even though the reflected shock wave of the ROSW is much smaller than that of the CJ ODW. According to Ben–Dor [26], this shock wave reflection phenomenon is called overall Mach Reflection (oMR).

As noted in the R–H analysis, the difference between P_{CJODW} and $P_{\mathrm{det,ODW}}$ decreases with increasing M. Therefore, the influence of the CJ ODW on the ODW weakens with increasing M. In the numerical results, as shown in Fig. 5, the size of the ROSW decreases with increasing M, and the reflection of the ROSW weakens with increasing M as well. Figure 6 shows the pressure field and pressure profiles along constant y coordinates of the ODW at $\theta = 25°$ and $M = 7.5$. It is observed that there is still a region behind the ODW in which the pressure is higher than its detachment pressure $P_{\mathrm{det,ODW}}$. Therefore, the ODW moves forward from the link point between itself and the CJ ODW, and the ROSW is formed as in the case of $M = 7.0$. Comparing Figs. 4b and 6b, it can be seen that the size of the region, in which the pressure is higher than $P_{\mathrm{det,ODW}}$, of Fig. 6b is much smaller than that of Fig. 4b. As a result, the detachment level is much weaker at $M = 7.5$, and the size of the ROSW is much shorter. In contrast to the case of $M = 7.0$, the reflection of the ROSW is not observed at $M = 7.5$. At the same time, the height of the Mach stem is much shorter than that of $M = 7.0$, even though the reflection of the CJ ODW is still a Mach reflection. In conclusion, instead of oMR, only the Mach reflection of the CJ ODW is observed at $M = 7.5$.

Figure 7 shows the pressure field and pressure profiles along constant y coordinates of the ODW at $\theta = 25°$ and $M = 8.4$. It is observed in Fig. 7b that the pressure of the flow field behind the ODW is below its detachment pressure $P_{\mathrm{det,ODW}}$. Thus, the ODW does not move forward as it does

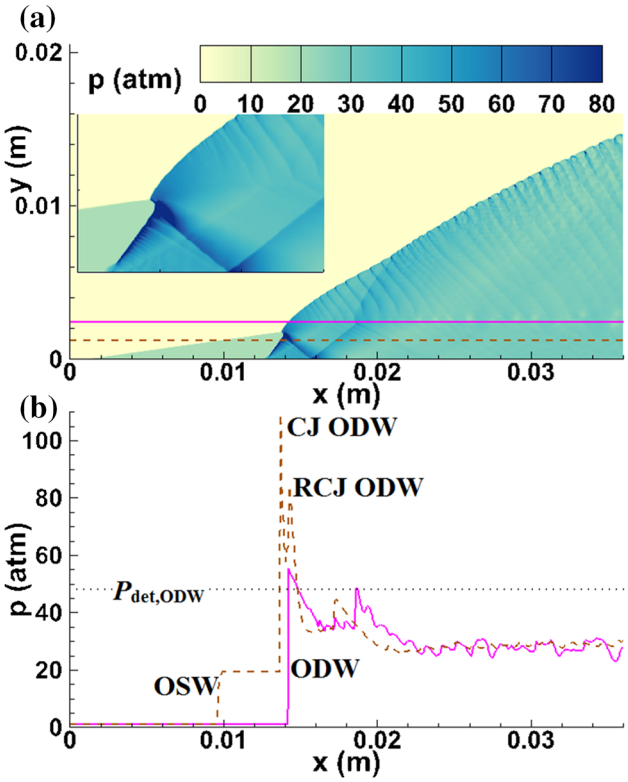

Fig. 6 Pressure field and pressure profiles of the ODW at $\theta = 25°$ and $M = 7.5$. The pressure profiles in the *second panel* are plotted *along the lines* shown in the *first panel*

in the cases of $M = 7.0$ and 7.5 and, therefore, the ROSW disappears in this case. Furthermore, the Mach stem above the CJ ODW also disappears, and then the reflection of the CJ ODW becomes a regular reflection. Similar to the model proposed by Ghorbanian and Sterling [5], the CJ ODW connects with the ODW directly as shown in Fig. 7a. A similar phenomenon is also observed in the numerical results of Teng et al. [19] with a detailed chemical reaction model.

With a further increase of M, it is observed that the RCJ ODW becomes weaker. Figure 8 shows the pressure field of the ODW at $\theta = 25°$ and $M = 9.0$. Similar to the case of $M = 8.4$, it is observed in Fig. 8 that the CJ ODW connects with the ODW directly. However, the RCJ ODW disappears. In other words, no reflection of the CJ ODW takes place in this case. Since the RCJ ODW is not observed in this

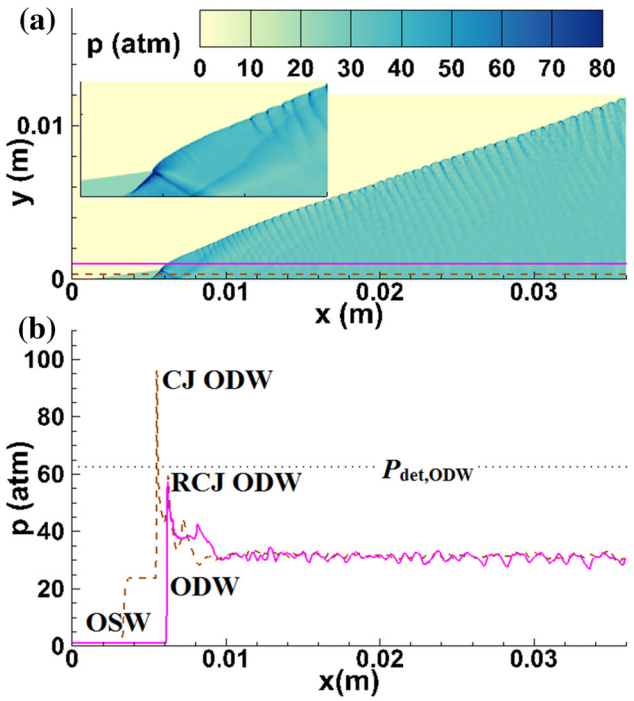

Fig. 7 Pressure field and pressure profiles of the ODW at $\theta = 25°$ and $M = 8.4$. The pressure profiles in the *second panel* are plotted *along the lines* shown in the *first panel*

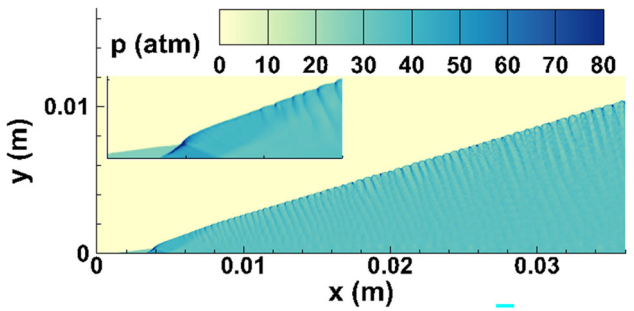

Fig. 8 Pressure field of the ODW at $\theta = 25°$ and $M = 9.0$

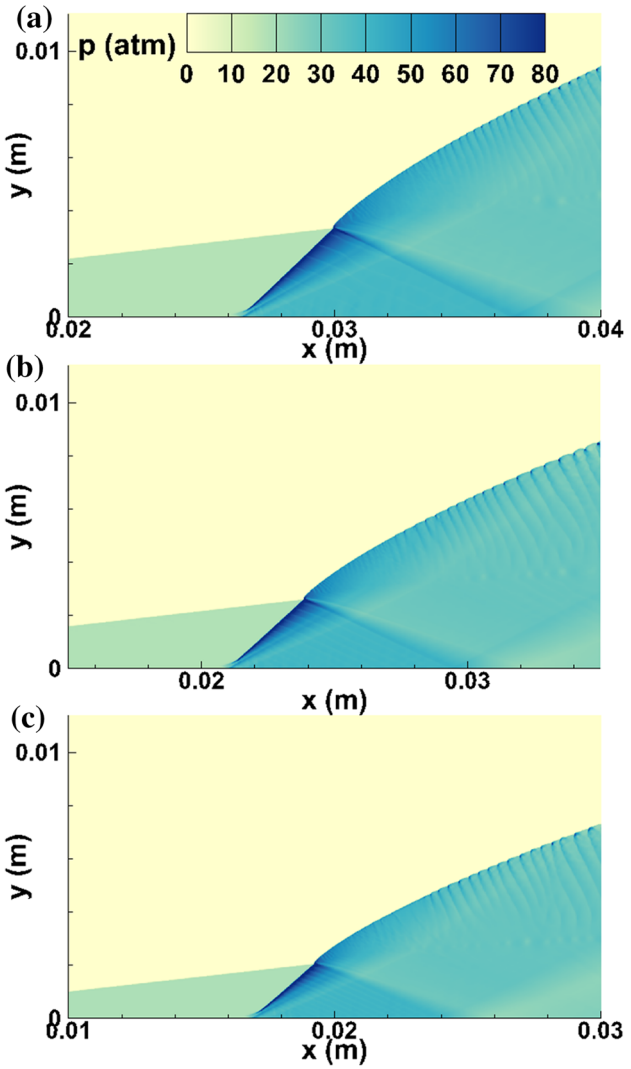

Fig. 9 Pressure fields of the ODWs at wedge angle $\theta = 21°$ and $M =$ **a** 8.4, **b** 8.6, and **c** 8.8

case, it is called non-reflection. A similar phenomenon is also observed, when the inflow Mach number is high enough, in the numerical results with the wedge angle ranging from 20° to 28°.

3.3 Disappearance mechanism of RCJ ODW

According to Figueira da Silva and Deshaies [27], the decrease of the wedge angle can lengthen the induction region and, consequently, extend the size of the CJ ODW. To facilitate observation, the ODW with $\theta = 21°$ is adopted to illustrate the mechanism of the disappearance of the RCJ ODW. Figure 9 shows the pressure fields of the ODWs at $\theta = 21°$ and $M = 8.4$, 8.6, and 8.8. As observed in Fig. 9, the RCJ ODW becomes weaker with increasing M. Similar to the phenomenon observed in Fig. 8, the RCJ ODW can only be observed in the vicinity of the reflection point in Fig. 9c. The CJ ODW angles at $\theta = 21°$ and $M = 8.4$, 8.6, and 8.8 are 43.9°, 42.3°, and 41.3°, respectively. They decrease gradually with the increase of M. The CJ ODW angles are in good agreement with the corresponding solutions of the R–H equations, which are 43.6°, 42.5°, and 41.4°, respectively. It can be concluded that the weakening of the RCJ ODW may partially result from the decrease of the CJ ODW angle.

In Fig. 9, it is also observed that the RCJ ODW becomes weaker as it moves away from the reflection point. Further, the RCJ ODW is slightly curved in the vicinity of the reflection point which is a typical phenomenon that a shock wave passing through an expansion wave presents. Figure 10 shows the velocity field and pressure field near the CJ ODW at $M = 8.6$ and $\theta = 21°$. As shown in Fig. 10a, the combustion products of the ODW and the CJ ODW are

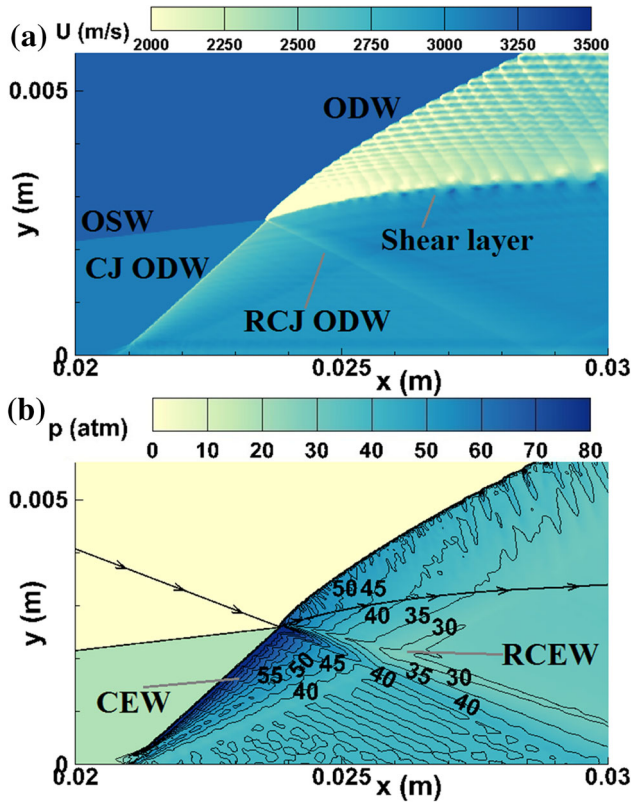

Fig. 10 **a** velocity field and **b** pressure field near the CJ ODW of the ODW at $M = 8.6$ and $\theta = 21°$. The *directing curve* is a *streamline*

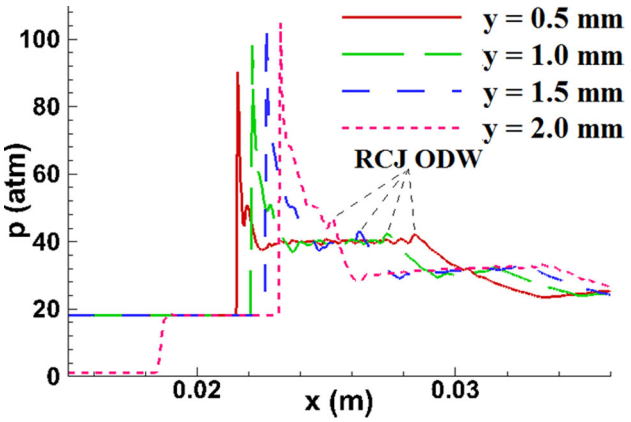

Fig. 11 Pressure distributions of the ODW at $M = 8.6$ and $\theta = 21°$ along $y = 0.5$, 1.0, 1.5, and 2.0 mm

separated by a shear layer. A CEW is observed behind the CJ ODW in Fig. 10b. As discussed, the RCJ ODW is curved under the influence of the CEW. Furthermore, as shown in Fig. 10b, the RCJ ODW is dramatically weakened when it passes through the CEW. The directing curve in Fig. 10b is the streamline across the link point of the ODW and the CJ ODW which can also approximately denote the shear layer shown in Fig. 10a. The CEW having transmitted through the RCJ ODW will partially transmit through and partially reflect from this shear layer [26]. The reflected expansion wave of the CEW (RCEW) which follows the RCJ ODW can be observed in Fig. 10b. The RCEW is always much weaker than the CEW, but it still plays a role in weakening the RCJ ODW.

Figure 11 shows the pressure distributions of the ODW at $M = 8.6$ and $\theta = 21°$ along different y coordinates. It can be observed that the upstream and downstream pressures of the RCJ ODW near the reflection point, namely at $y = 2.0$ mm, are both greater than those at smaller y coordinates. This results from the fact that the expansion process performed by the CEW on the CJ ODW combustion products is not completed near the reflection point. Further, the weakening effect of the CEW on the RCJ ODW is not completed. Therefore, the upstream and downstream pressures of the RCJ ODW in the CEW are both higher than those outside the CEW as shown in Figs. 9 and 10b. At smaller y coordinates ($y = 0.5$, 1.0, and 1.5 mm) where the expansion process of the CJ ODW combustion products is completed, it is observed that the upstream pressures of the RCJ ODW are almost the same. However, the post-shock pressures of the RCJ ODW decrease with decreasing y coordinate as noted in Fig. 11. The RCJ ODW gradually weakens as it comes to the wedge surface under the weakening effect of the RCEW. Therefore, it can be concluded that, in addition to the CEW, the RCEW plays a role in the disappearance of the RCJ ODW.

To investigate the influence of the inflow Mach number and wedge angle on the disappearance of the RCJ ODW, the numerical simulations are performed with the wedge angle ranging from 20° to 28° with 1° intervals. The numerical results show that the RCJ ODWs at $\theta = 20°$, 21°, 22°, 24°, 26°, and 28° can take place at $M = 8.6$, but they disappear at $M = 8.8$. The RCJ ODWs at $\theta = 23°$, 25°, and 27° can take place at $M = 8.8$, but they disappear at $M = 9.0$. Therefore, the critical Mach number of the disappearance of the RCJ ODW is between 8.6–8.8 at $\theta = 20°$, 21°, 22°, 24°, 26°, and 28°, and between 8.8–9.0 at $\theta = 23°$, 25°, and 27°. The change of critical inflow Mach number, which is always at about $M = 8.8$, is small when the wedge angle is changed. Therefore, the inflow Mach number is a dominant parameter in the disappearance process of the RCJ ODW. Because the disappearance of the RCJ ODW results from the interaction among the RCJ ODW, CEW, and RCEW, it is a formidable task to use an analytical method to describe the influence of the inflow Mach number and wedge angle on the disappearance of the RCJ ODW.

4 Conclusions

ODW structures are investigated via numerical simulations and R–H analysis. The two-dimensional Euler equations cou-

pled with a two-step chemical reaction model are solved. According to the R–H analysis, the interaction between the CJ ODW and ODW should become weaker with an increase in M. This tendency is also seen in the numerical results. As the inflow Mach number increases, four configurations of the wave reflection of the CJ ODW are observed, i.e., overall Mach reflection, Mach reflection, regular reflection, and non-reflection.

At $M = 7.0$ and $\theta = 25°$, under the influence of the CJ ODW, the ODW is partially detached and an ROSW forms. The CJ ODW collides with the ROSW and then forms an oMR wave configuration. Because the detachment level of the ODW weakens with increasing M, the size of the ROSW decreases with increasing M. At $M = 7.5$ and $\theta = 25°$, the reflection of the ROSW disappears and, consequently, the oMR becomes a Mach reflection of the CJ ODW. At $M = 8.4$ and $\theta = 25°$, the reflection of the CJ ODW becomes a regular reflection. Furthermore, the RCJ ODW becomes weaker with increasing M. At about $M = 8.8$, the RCJ ODW disappears under the weakening effect of the CEW and RCEW. Since no RCJ ODW is observed in this case, it is called non-reflection.

Acknowledgments This work was sponsored by the National Natural Science Foundation of China (No. 91441110).

References

1. Kailasanath, K.: Review of propulsion applications of detonation waves. AIAA J. **38**(9), 1698–1708 (2000)
2. Ma, F., Choi, J.-Y., Yang, V.: Propulsive performance of air breathing pulse detonation engines. J. Propuls. Power **22**(6), 1188–1203 (2006)
3. Dunlap, R., Brehm, R.L., Nicholls, J.A.: A preliminary study of the application of steady-state detonative combustion to a reaction engine. J. Jet Propuls. **28**(7), 451–456 (1958)
4. Pratt, D.T., Humphrey, J.W., Glenn, D.E.: Morphology of standing oblique detonation waves. J. Propuls. Power **7**(5), 837–845 (1991)
5. Ghorbanian, K., Sterling, J.D.: Influence of formation processes on oblique detonation wave stabilization. J. Propuls. Power **12**(3), 509–517 (1996)
6. Li, C., Kailasanath, K., Oran, E.S.: Detonation structures behind oblique shocks. Phys. Fluids **6**(4), 1600–1611 (1994)
7. Choi, J.-Y., Kim, D.-W., Jeung, I.-S., Ma, F., Yang, V.: Cell-like structure of unstable oblique detonation wave from high-resolution numerical simulation. Proc. Combust. Inst. **31**(2), 2473–2480 (2007)
8. Wang, A.-F., Zhao, W., Jiang, Z.-L.: Cellular structure of oblique detonation and propagation of transverse wave. Explos. Shock Waves **30**(4), 349–354 (2010)
9. Gui, M.-Y., Fan, B.-C., Dong, G.: Periodic oscillation and fine structure of wedge-induced oblique detonation waves. Acta Mech. Sin. **27**(6), 922–928 (2011)
10. Verreault, J., Higgins, A.J., Stowe, R.A.: Formation of transverse waves in oblique detonations. Proc. Combust. Inst. **34**(2), 1913–1920 (2013)
11. Verreault, J., Higgins, A.J.: Initiation of detonation by conical projectiles. Proc. Combust. Inst. **33**, 2311–2318 (2011)
12. Lefebvre, M.H., Fujiwara, T.: Numerical modeling of combustion processes induced by a supersonic conical blunt body. Combust. Flame **100**, 85–93 (1995)
13. Liu, Y., Wu, D., Yao, S.-B., Wang, J.-P.: Analytical and numerical investigations of wedge-induced oblique detonation waves at low inflow Mach number. Combust. Sci. Technol. **187**(6), 843–856 (2015)
14. Dabora, E. K., Broda, J.-C.: Standing normal detonations and oblique detonations for propulsion. AIAA paper 93–2325 (1993)
15. Viguier, C., Gourara, A., Desbordes, D.: Three-dimensional structure of stabilization of oblique detonation wave in hypersonic flow. Proc. Combust. Inst. **27**(2), 2207–2214 (1998)
16. Maeda, S., Kasahara, J., Matsuo, A.: Oblique detonation wave stability around a spherical projectile by a high time resolution optical observation. Combust. Flame **159**, 887–896 (2012)
17. Ashford, S.A., Emanuel, G.: Wave angle for oblique detonation waves. Shock Waves **3**, 327–329 (1994)
18. Verreault, J., Higgins, A.J., Stowe, R.A.: Formation and structure of steady oblique and conical detonation waves. AIAA J. **50**(8), 1766–1772 (2012)
19. Teng, H.-H., Zhao, W., Jiang, Z.-L.: A novel oblique detonation structure and its stability. Chin. Phys. Lett. **24**(7), 1985–1988 (2007)
20. Li, C., Kailasanath, K., Oran, E. S.: Effects of boundary layers on oblique-detonation structures. In: 31st Aerospace Sciences Meeting & Exhibit, Reno, Nevada, AIAA-93-0450 (1993)
21. Kamel, M. R., Morris, C. I., Stouklov, I. G., Hanson, R. K.: PLIF imaging of hypersonic reactive flow around blunt bodies. In: 26th International Symposium on Combustion, Combustion Institute, Pittsburg, pp. 2909–2915 (1996)
22. Korobeinikov, V.P., Levin, V.A., Markov, V.V., Chernyi, G.G.: Propagation of blast waves in a combustible gas. Astronaut. Acta **17**(4–5), 529–537 (1972)
23. Liu, Y.-F.: Numerical Studies on Detonation and Pulse Detonation Engines. Peking University, Beijing (2004)
24. Steger, J.L., Warming, R.F.: Flux vector splitting of the inviscid gasdynamic equations with application to finite-difference methods. J. Comput. Phys. **40**(2), 263–293 (1981)
25. Balsara, D.S., Shu, C.-W.: Monotonicity preserving weighted essentially non-oscillatory schemes with increasingly high order of accuracy. J. Comput. Phys. **160**(2), 405–452 (2000)
26. Ben-Dor, G.: Shock Wave Reflection Phenomena, 2nd edn. Springer, New York (2007)
27. da Silva, L.F.F., Deshaies, B.: Stabilization of an oblique detonation wave by a wedge: a parametric numerical study. Combust. Flame **121**, 152–166 (2000)